



Large Eddy Simulation of Thermally Stratified Atmospheric Boundary Layers with a Lattice Boltzmann Method

Henry Korb¹, Henrik Asmuth¹, Martin Schönherr², Martin Geier², and Stefan Ivanell¹

¹Wind Energy Division, Department of Earth Sciences, Uppsala University, Visby, Sweden

Correspondence: Henry Korb (henry.korb@geo.uu.se)

Abstract. Thermal stratification plays an important role in wind farm flows and must therefore be included in simulations of such flows. Meanwhile, wind farms are covering larger areas, requiring very large domains and leading to exceptional computational costs for Large Eddy Simulation (LES). The lattice Boltzmann method (LBM) is a novel approach to LES of wind farm flows that is particularly efficient and suitable for massively parallel hardware, such as GPUs (graphics processing units). In this work we present a novel model for LES-LBM of stratified atmospheric boundary layers, using a so-called double distribution function approach. We develop a novel boundary condition to apply Monin-Obukhov similarity theory and implement a number of other components required for simulations of stratified boundary layers in the GPU-resident version of the open-source LBM solver VIRTUALFLUIDS. The model is validated for conventionally neutral and stably stratified boundary layers. Results agree closely with numerical references. The model is able to simulate conventionally neutral boundary layers at around realtime on a single GPU. Future work will include development of a precursor-successor method for wind farm flow simulations and improvements to the collision operator of temperature model.

1 Introduction

In 2019, the wind farm developer Ørsted announced that it had to reduce projected lifetime returns for multiple large offshore wind farms by 0.5 percentage points. Having long noticed an under-performance of their assets, an internal investigation revealed that this underestimation was due to an underestimation of blockage and wake effects in their models (Ørsted, 2019). The example of Ørsted shows that current state of the art models used in the wind energy industry are incapable of accounting for the complexity of the atmospheric boundary layer and that more accurate models are needed to reduce risks and in turn reduce costs in the wind energy sector.

It is now understood that an additional form of blockage, named hydrostatic blockage, occurs when large wind farms trigger gravity waves in the stably stratified free atmosphere. These waves can result in unfavorable pressure gradients in front of the wind farm, as demonstrated in a range of LES (Large Eddy Simulation) by, for example, Lanzilao and Meyers (2022, 2024) or Wu and Porté-Agel (2017). However, gravity waves can only exist if parts of the atmosphere are stably stratified and thus can only be observed in LES if buoyancy effects are included in the LES model. Furthermore, the examination of gravity waves requires very large domains with high resolution, since the wavelengths are on the order of tens of kilometers, while

²Institute for Computational Modeling in Civil Engineering, TU Braunschweig, Braunschweig, Germany

https://doi.org/10.5194/wes-2025-181
Preprint. Discussion started: 20 October 2025







grid spacings of around 5m are required for accurate resolution of the wall and inversion layer, as discussed, in Allaerts and Meyers (2017). The resulting simulations thus feature extremely large numbers of degrees of freedom. Current LES models for the atmospheric boundary layer, typically CPU-resident finite volume or pseudospectral solvers, require days or months of computing time on very large compute clusters to perform such simulations.

A new generation of solvers seek to alleviate the immense computational cost by utilizing GPUs (Graphics Processing Units), such as MIRCOHH (van Heerwaarden et al., 2017), AMR-WIND (Kuhn et al., 2025) and FASTEDDY (Sauer and Muñoz-Esparza, 2020). van Heerwaarden et al. (2017) report that 32 CPU cores are necessary to achieve the computational performance as one NVIDIA Quadro K6000. Sauer and Muñoz-Esparza (2020) already report that one GPU equals the performance of 256 CPU cores, highlighting the rapidly increasing speed of GPUs.

However, a different approach, based on the lattice Boltzmann method (LBM), was also introduced to wind energy and boundary layer research over the last decade. The LBMs mathematical structure is well suited for the use of massively parallel hardware, such as GPUs. The LBM can be thought of as a two-step algorithm. First, populations at a node collide and are then advected to neighboring nodes (Krüger et al., 2017). The collision step is potentially non-linear but is a local operation, while the advection step simply consists of moving memory on a computer. While initial formulations of the LBM were unstable at high Reynolds numbers, recent advances in the formulation of the collision step have rendered it a suitable method for high-Reynolds flows and LES (Geier et al., 2015, 2020; Jacob et al., 2018).

LES based on the LBM has been used now for over a decade to simulate large-scale boundary layer flows. Onodera et al. (2013) present a simulation of $10 \text{km} \times 10 \text{km}$ of Tokyo's urban area at a 1 m resolution on up to 1000 GPUs, demonstrating the methods suitability for very large problems. Further examples of simulations utilizing GPUs include King et al. (2017) and Lenz et al. (2019). Both report near realtime computational performance, demonstrating the high computational efficiency of the LBM on GPUs. None of the aforementioned simulations include wall models. Asmuth et al. (2021) introduced a wall-modeling approach suitable for atmospheric boundary layers and presented very good agreement with reference results.

All of the aforementioned models only consider isothermal boundary layers and very few models considering thermal stratification have been previously presented in the literature. The temperature equation can be discretized either via "traditional" approaches, such as finite difference or finite volume, or via a modified LBM. The former is named a hybrid approach while the latter is referred to as a double-distribution-function approach (DDF). A hybrid approach was applied in one of the earliest studies of stratified boundary layer flows with the LBM, the THELMA project, described in a series of publications (Obrecht et al., 2012, 2013, 2015). Another solver designed for atmospheric boundary layers implementing a hybrid approach is presented in Feng et al. (2021). PROLB employs the hybrid recursive regularized collision model (Jacob et al., 2018) and the wall-modeling approach by Malaspinas and Sagaut (2014). However, it is not mentioned that it utilizes GPUs and no remarks on its computational performance are given. An overview of advection-diffusion LBM models can be found in Gruszczyński and Łaniewski-Wołłk (2022), where the authors also compare a number of more advanced LBM models. They find that models based on the cascaded LBM yield the most accurate results. A similar model is applied in Alihussein et al. (2021) to simulate the dissolution in porous media. Wang et al. (2020) present a method using the DDF approach for simulation of the





stratified flow over a ridge. Both LBM models (for momentum and temperature), employ a multiple-relaxation time method (d'Humières, 1994).

In this paper, we propose a novel model to simulate the stratified atmospheric boundary layer via a DDF LBM model based on the cumulant LBM for momentum and a factorized cascaded model for the advection diffusion equation. We describe the methodology in section 2. We compare results obtained with our method to reference data for each a neutral and a stably stratified test case in section 3 and give our concluding remarks in section 4. As with any model development, we have tried many different variants until we converged on the model we present here. We document some of those approaches in Appendix A.

2 Methodology

We will be begin by describing the fundamentals of the cumulant Lattice Boltzmann method and its modifications to simulate atmospheric boundary layers. Subsequently, we present the method used to simulate the advection-diffusion of the potential temperature. Finally we discuss novel formulations for boundary conditions and other aspects specific to modeling thermally stratified boundary layers.

2.1 Governing equations

Our aim is to simulate the filtered incompressible Navier-Stokes equations with Coriolis forces coupled to an advection-diffusion equation of potential temperature via the Boussinesq approximation (Stoll et al., 2020):

$$\frac{\partial u_i}{\partial x_i} = 0 \tag{1}$$

$$\frac{\partial u_i}{\partial t} + u_j \frac{\partial u_i}{\partial x_j} = -\frac{1}{\rho_0} \frac{\partial p}{\partial x_i} + \frac{\partial}{\partial x_i} \left(\nu_e \frac{\partial u_j}{\partial x_j} \right) + F_i^C + F_i^B$$
(2)

$$\frac{\partial \theta}{\partial t} + u_j \frac{\partial \theta}{\partial x_j} = \frac{\partial}{\partial x_j} \left(D_e \frac{\partial \theta}{\partial x_j} \right). \tag{3}$$

Here, the coordinate system is denoted as $\boldsymbol{x} = [x, y, z]^T$, t is time, ρ_0 is the density, \boldsymbol{u} is the filtered velocity, p is the pressure deviation from the background pressure, θ is the filtered potential temperature, the Coriolis and buoyancy force are \boldsymbol{F}^C and \boldsymbol{F}^B , respectively, and subgrid stresses and heat flux are parameterized via an effective viscosity and diffusivity, ν_e and D_e , respectively. We use Einstein summation convention. The Coriolis force is given by

$$F_i^{\mathcal{C}} = -\epsilon_{ij3} \left(G_j - u_j \right) f_{\mathcal{C}},\tag{4}$$

where ϵ_{ijk} is the Levi-Civita symbol, $G = G[\cos \alpha, \sin \alpha, 0]^T$ is the geostrophic wind with the geostrophic wind speed G and direction α , and f_c is the Coriolis parameter. The buoyancy force is computed according to

85
$$F_i^{\rm B} = g \frac{\theta - \langle \theta \rangle(z)}{\theta_{\rm r}} \delta_{i3},$$
 (5)





where g is the gravitational acceleration, $\langle \cdot \rangle$ signifies horizontal averaging, θ_r is a reference temperature and δ_{ij} is the Kronecker delta. Contrary to "classical" computational fluid dynamics, we do not discretize these equations but instead solve them via the lattice Boltzmann method implemented in the GPU-resident version of the open-source solver VIRTUALFLUIDS (Geier et al., 2025).

2.2 The Cumulant Lattice Boltzmann Method

The fundamental variable of the lattice Boltzmann method is the particle distribution function (PDF) f. The PDF describes the probability of encountering a particle with velocity ξ at time t and location x. The discretization of velocity space to a lattice of discrete velocities $c_{\iota\kappa\lambda} = (\iota\delta_{i1} + \kappa\delta_{i2} + \lambda\delta_{i3})c$ with $c = \frac{\Delta x}{\Delta t}$ as lattice velocity, leads to the discrete populations $f_{\iota\kappa\lambda}(x,t) := f(c_{\iota\kappa\lambda},x,t)$. Following Geier et al. (2015), we denote lattice directions with triplets of Greek indices corresponding to their directions in space and define $\bar{\iota} := -\iota$. Note that Greek indices are not subject to the summation convention and triplet indices in parentheses represent all possible permutations of that triplet. We employ a D3Q27 lattice, i.e. the set of 27 lattice directions of all permutations with $\iota,\kappa,\lambda\in\{-1,0,1\}$. The lattice speed of sound is $c_{\rm s}=\frac{c}{\sqrt{3}}$ and each $c_{\iota\kappa\lambda}$ has an associated weight $w_{\iota\kappa\lambda}$. Macroscopic quantities, that is quantities on the scale of continuum mechanics, are obtained by taking different order moments of $f_{\iota\kappa\lambda}$, for example density (zeroth-order) and velocity (first-order):

$$100 \qquad \rho = \sum f_{\iota\kappa\lambda} \tag{6}$$

$$\rho \mathbf{u} = \sum \mathbf{c}_{\iota\kappa\lambda} f_{\iota\kappa\lambda} + \frac{\mathbf{F}}{2}.\tag{7}$$

 ${m F}$ is the total force density. The evolution of the PDF is described by the Boltzmann equation. Replacing the continuous PDFs with the discrete populations and integration along the characteristic ${m x}={m c}_{\iota\kappa\lambda}t$ from t to $t+\Delta t$ yields the lattice Boltzmann equation

105
$$f_{\iota\kappa\lambda}(\mathbf{x} + \mathbf{c}_{\iota\kappa\lambda}\Delta t, t + \Delta t) = f_{\iota\kappa\lambda}(\mathbf{x}, t) + \Delta t\Omega_{\iota\kappa\lambda}(\mathbf{x}, t),$$
 (8)

where Ω is the collision operator, that will be discussed later on. Asymptotic analysis shows that the moments of the lattice Boltzmann equation yield the weakly compressible Navier-Stokes equations, which approximates the incompressible Navier-Stokes equations with an error proportional to $\mathcal{O}(\mathrm{Ma^3})$, with the Mach number $\mathrm{Ma} = \frac{V_0}{c_\mathrm{s}}$ and V_0 a reference velocity. The size of this error is effectively controlled by the size of the time step and the grid spacing since

110 Ma =
$$\frac{\sqrt{3}V_0\Delta t}{\Delta x}$$
. (9)

By limiting Ma < 0.1 we ensure that the error is small. The collision operator is of great importance for the accuracy and stability of the method. In this work we employ the cumulant collision operator (Geier et al., 2015, 2017), here we present a short overview. Generally, collision operators relax the populations towards an equilibrium. The cumulant collision operator performs this relaxation in cumulant space, eliminating many shortcomings of traditional multi-relaxation time methods, mainly due to the fact that cumulants are statistically independent and can therefore be relaxed at independent rates. First, the



135



populations in continuous form undergo a Laplace transformation to wave number space:

$$F(\Xi) = \mathcal{L}\left\{\sum_{\iota\kappa\lambda} f_{\iota\kappa\lambda}\delta(\iota c - \xi)\delta(\kappa c - \upsilon)\delta(\lambda c - \zeta)\right\},\tag{10}$$

where δ is the Dirac delta function. Thereafter, cumulants $c_{\alpha\beta\gamma}$ are obtained from the cumulant generating function

$$c_{\alpha\beta\gamma} = c^{-\alpha-\beta-\gamma} \frac{\partial^{\alpha}\partial^{\beta}\partial^{\gamma}}{\partial \Xi^{\alpha}\partial \Upsilon^{\beta}\partial Z^{\gamma}} \ln(F(\Xi)) \bigg|_{\Xi=\Upsilon=Z=0}.$$
 (11)

Note that transformation from populations to cumulants is implemented via the chimera transform, which greatly reduces the computational cost while significantly improving the numerical precision of the computation, (Geier et al., 2015, Appendix I). After transformation, the cumulants are relaxed towards their respective equilibrium $c_{\alpha\beta\gamma}^{\rm eq}$:

$$c_{\alpha\beta\gamma}^* = \omega_{\alpha\beta\gamma} c_{\alpha\beta\gamma}^{\text{eq}} + (1 - \omega_{\alpha\beta\gamma}) c_{\alpha\beta\gamma},\tag{12}$$

where $c_{\alpha\beta\gamma}^*$ denotes the post-collision cumulant. Finally, the post-collision cumulants are transformed back to populations. The relaxation rates $\omega_{\alpha\beta\gamma}$ are computed according to Geier et al. (2017). The relaxation rate of the second order cumulants $\omega_{(110)}$ is related to the kinematic viscosity by

$$\frac{1}{\omega_{(110)}} = \frac{\nu}{c_{\rm s}^2 \Delta t} + \frac{1}{2}.\tag{13}$$

In this study, we employ an eddy-viscosity model to explicitly model the subgrid scales of the LES. Some studies, e.g. Geier et al. (2020) or Gehrke and Rung (2022) suggest to use the cumulant operator alone to conduct implicit LES. However, we have found this method unsuitable for performing LES of the atmospheric boundary layer due to the very high Reynolds number, as discussed in Asmuth et al. (2021).

2.3 The Lattice Boltzmann Method for Advection-Diffusion

To solve the advection-diffusion equation, one can either use a so-called hybrid solver, that solves the Navier-Stokes equations via the LBM and the advection-diffusion equation via finite differences or the finite volume method. The other possibility is to use another LBM solver to solve the advection-diffusion equation with a double distribution function (DDF) approach. The hybrid method has the advantage that it requires significantly less memory, since for every node in the grid we only have to save one quantity, as compared to the DDF, which needs to save 27 (if one uses a D3Q27 lattice) quantities per node. Therefore, we also implemented a hybrid approach first but despite much effort it was not successful. We discuss the details of the approaches we tried in Appendix A. Instead, we pivoted to a DDF approach:

We can describe a scalar, such as the potential temperature θ , with a second set of populations, $g_{\iota\kappa\lambda}$, and define:

$$\theta = \sum g_{\iota\kappa\lambda}.\tag{14}$$

During collision, only the zeroth-order moment, i.e. θ , is conserved. The lattice Boltzmann equation for the advection-diffusion problem is analogous to the formulation for momentum:

$$g_{\iota\kappa\lambda}(\boldsymbol{x} + \boldsymbol{c}_{\iota\kappa\lambda}\Delta t, t + \Delta t) = g_{\iota\kappa\lambda}(\boldsymbol{x}, t) + \Delta t \Omega_{\iota\kappa\lambda}^{\mathrm{AD}}(\boldsymbol{x}, t). \tag{15}$$





In this work, we employ the factorized central moment based collision operator described in Yang et al. (2016). Similar to the cumulant method, the populations $g_{\iota\kappa\lambda}$ first undergo a Laplace transform

$$G(\Xi) = \mathcal{L}\left\{ \sum_{\iota \kappa \lambda} g_{\iota \kappa \lambda} \delta(\iota c - \xi) \delta(\kappa c - \upsilon) \delta(\lambda c - \zeta) \right\}. \tag{16}$$

Central moments $\tilde{\kappa}$ are then obtained from the moment generating function

$$\tilde{\kappa}_{\alpha\beta\gamma} = c^{-\alpha-\beta-\gamma} \frac{\partial^{\alpha}\partial^{\beta}\partial^{\gamma}}{\partial\Xi^{\alpha}\partial\Upsilon^{\beta}\partial\mathsf{Z}^{\gamma}} e^{-\boldsymbol{u}\cdot\boldsymbol{\Xi}} G(\boldsymbol{\Xi}) \bigg|_{\boldsymbol{\Xi}=\Upsilon=\mathsf{Z}=0}.$$
(17)

Again, the computation is performed via the chimera transform. To obtain the factorized central moments $\kappa_{\alpha\beta\gamma}$, the following orthogonalization is applied:

$$\kappa_{000} = \tilde{\kappa}_{000}$$

$$\kappa_{(100)} = \tilde{\kappa}_{(100)}$$

$$\kappa_{(110)} = \tilde{\kappa}_{(110)}$$

155
$$\kappa_{111} = \tilde{\kappa}_{111}$$

$$\kappa_{(200)} = \tilde{\kappa}_{(200)} - \frac{1}{3}\kappa_{000}$$

$$\kappa_{(210)} = \tilde{\kappa}_{(210)} - \frac{1}{3}\kappa_{(010)}$$

$$\kappa_{(211)} = \tilde{\kappa}_{(211)} - \frac{1}{3} \kappa_{(011)}$$

$$\kappa_{(220)} = \tilde{\kappa}_{(220)} - \frac{1}{3}\kappa_{000}$$

$$\mathbf{160} \quad \kappa_{(221)} = \tilde{\kappa}_{(221)} - \frac{1}{9} \kappa_{(001)}$$

$$\kappa_{222} = \tilde{\kappa}_{222} - \frac{1}{27} \kappa_{000}.$$

The factorized central moments are then relaxed towards their equilibria

$$\kappa_{\alpha\beta\gamma}^* = \omega_{\alpha\beta\gamma}\kappa_{\alpha\beta\gamma}^{eq} + (1 - \omega_{\alpha\beta\gamma})\kappa_{\alpha\beta\gamma}.$$
 (18)

All equilibria are zero, except

165
$$\kappa_{(200)}^{\text{eq}} = c_{\text{s}}^2 \kappa_{000}$$
 (19)

$$\kappa_{(220)}^{\text{eq}} = c_{\text{s}}^4 \kappa_{000} \tag{20}$$

$$\kappa_{(222)}^{\text{eq}} = c_{\text{s}}^6 \kappa_{000}.$$
(21)

The first order relaxations are related to the diffusivity by

$$\frac{1}{\omega_{(100)}} = \frac{D}{c_{\rm s}^2 \Delta t} + \frac{1}{2},\tag{22}$$

while we set all other relaxation rates to one. After the relaxation, the factorized central moments have to be transformed back to central moments and then populations.



180



2.4 Boundary Conditions

We require two boundary conditions for the fluid and potential temperature field each. At the top of the domain we set a slip condition for the fluid flow and either a Neumann or Dirichlet type boundary condition for potential temperature. At the bottom we will set a combined stress and flux boundary condition computed from a wall model that will be discussed in subsection 2.5. Boundary conditions in the LBM have to be specified for the populations, therefore a variety of methods can be found resulting in the same macroscopic boundary condition. For the sake of completeness we describe the boundary conditions for the fluid in more detail in Appendix B. A Dirichlet type boundary condition for the scalar can be implemented via the anti bounce-back rule as described in Krüger et al. (2017, p. 318). A Neumann boundary condition can be implemented via this approach as well. However, in preliminary studies we found this approach to cause spurious oscillations at the top of the domain.

Instead, we present here a formulation for a flux boundary condition, that will also be used as a Neumann boundary condition at the top of the domain. We first recall a few basic relations. The total flux j is the sum of the diffusive and advective fluxes j^{D} and j^{A} :

$$j = j^{D} + j^{A} = -D\nabla\theta + u\theta. \tag{23}$$

Our goal is now to set a specified wall flux q_w , which will either be computed from a wall model, or, in case of a Neumann boundary condition from $q_w = -D\frac{\partial \theta}{\partial n}$, where $\frac{\partial \theta}{\partial n}$ is the specified gradient in wall normal direction n, with n pointing into the fluid domain.

We compute the diffusive flux at the node from the first order moment of g:

$$j_i^{\rm D} = \sum g_{\iota\kappa\lambda} c_{\iota\kappa\lambda,i} - u_i \theta. \tag{24}$$

We then prescribe the flux at the wall j^{w} to be equal to the diffusive flux in the tangential direction and equal to q_{w} in the wall normal direction:

$$j_i^{\text{W}} = j_i^{\text{D}} - (j_j^{\text{D}} n_j) n_i + q_{\text{w}} n_i.$$
 (25)

Finally, we employ the bounce back rule to compute the missing distributions $g_{\overline{\iota\kappa\lambda}}$:

$$g_{\overline{\iota\kappa\lambda}} = g_{\iota\kappa\lambda} - 2w_{\iota\kappa\lambda} \frac{c_{\iota\kappa\lambda,i} j_i^{\mathrm{W}}}{c_s^2}.$$
 (26)

195 2.5 Wall Model

At the bottom boundary, we make use of the standard Monin-Obukhov similarity theory (MOST) to determine the wall shear-stress $\tau_{\rm w}$ and heat flux $q_{\rm w}$:

$$\zeta(z) = \frac{z}{L} = -\frac{z\kappa g q_{\rm w}}{u_*^3 \theta_{\rm r}} \tag{27}$$

$$u(z) = \frac{u_*}{\kappa} \left(\ln \frac{z}{z_0} - \psi_{\rm M}(\zeta) \right) \tag{28}$$

200
$$\theta(z) - \theta_0 = -\frac{q_{\rm w}}{u_* \kappa} \left(\ln \frac{z}{z_{0,\rm H}} - \psi_{\rm H}(\zeta) \right), \tag{29}$$





where ζ is a stability parameter based on the Obukhov length L, $u_* = \sqrt{\frac{\tau_{\rm w}}{\rho}}$ is the friction velocity, κ is the von-Kàrmàn constant, z_0 and $z_{0,\rm H}$ are roughness lengths for momentum and temperature, respectively, and θ_0 is the surface temperature (Arya, 2001). The similarity functions for momentum $(\psi_{\rm M}(\zeta))$ and heat $(\psi_{\rm H}(\zeta))$ have to be determined experimentally. We use the classical Businger-Dyer relations (Businger et al., 1971)

205
$$\phi_{\rm M}^{-1}(\zeta) = (1 - \gamma_{\rm M} \zeta)^{1/4}$$
 (30)

$$\phi_{\rm H}^{-1}(\zeta) = (1 - \gamma_{\rm H}\zeta)^{1/2} \tag{31}$$

$$\psi_{M}(\zeta) = \begin{cases} \ln\left[\left(\frac{1+\phi_{M}^{-2}}{2}\right)\left(\frac{1+\phi_{M}^{-1}}{2}\right)^{2}\right] \\ -2\tan^{-1}\phi_{M}^{-1} + \frac{\pi}{2}, \quad \zeta < 0 \\ -\beta_{M}\zeta, \quad \zeta \ge 0 \end{cases}$$
(32)

$$\psi_{\mathrm{H}}(\zeta) = \begin{cases} 2\ln\left(\frac{1+\phi_{\mathrm{H}}^{-1}}{2}\right), & \zeta < 0\\ -\beta_{\mathrm{H}}\zeta, & \zeta \ge 0 \end{cases}$$
(33)

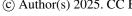
We set $\beta_{\rm M}=4.8$ and $\beta_{\rm H}=7.8$ according to Beare et al. (2006) and $\gamma_{\rm M}=\gamma_{\rm H}=15$ as suggested by Arya (2001). Based on a user-specified distance $z_{\rm EL}$, we sample an exchange-location temperature $\theta_{\rm EL}$ and velocity $u_{\rm EL}$. Additionally, the exchange-location quantities are exponentially averaged in time, as is recommended by Yang et al. (2017). The user can choose to either prescribe the surface heatflux or the surface temperature. We employ a variation of algorithm(1) or algorithm(2) from Basu et al. (2008), depending on the prescribed quantity, displayed in Algorithm 1. In the following, the subscript t denotes vectors tangential to the wall, overbars denote temporal averages and quantities at the first node in the fluid domain are denoted with the subscript 1.

Algorithm 1 Algorithm for computing wall shear stress and kinematic heat flux

$$\begin{split} &u_*^t \leftarrow u_*^{t-1}, q_{\mathrm{w}}^t \leftarrow q_{\mathrm{w}}^{t-1} \\ &\textbf{repeat} \\ &u_*^{\mathrm{Old}} \leftarrow u_*^t \\ &\text{compute } \zeta \text{ via (27)} \\ &\text{compute } \psi_{\mathrm{H}} \text{ and } \psi_{\mathrm{M}} \text{ via (32) and (33)} \\ &u_*^t = \kappa \overline{|u_{\mathrm{EL}}^t|} \left(\ln \frac{z_{\mathrm{EL}}}{z_0} - \psi_{\mathrm{M}} \right)^{-1} \\ &\textbf{if surface temperature given then} \\ &q_{\mathrm{w}}^t = -u_*^t \kappa \left(\overline{\theta_{\mathrm{EL}}} - \theta_0 \right) \left(\ln \frac{z_{\mathrm{EL}}}{z_{0,\mathrm{H}}} - \psi_{\mathrm{H}} \right)^{-1} \\ &\textbf{end if} \\ &\textbf{until } \frac{u_*^t - u_*^{\mathrm{Old}}}{u_*^{\mathrm{Old}}} < 10^{-4} \\ &\tau_{\mathrm{w}} = \rho(u_*^t)^2 \frac{u_{1,\mathrm{t}}}{|u_{1,\mathrm{t}}|} \end{split}$$

215

The combined boundary condition, which we named the *surface layer boundary condition* is executed in the following steps:







- 1. load $f_{\iota\kappa\lambda}^*$ at boundary node and compute ρ_1 and u_1 via (6) and (7)
- 2. load $g_{\iota\kappa\lambda}^*$ at boundary node and compute θ_1 via (14)
- 3. compute $\tau_{\rm w}$ and $q_{\rm w}$ according to Algorithm 1 using $u_{\rm EL}$, $\theta_{\rm EL}$, z_0 , $z_{0,\rm H}$, $z_{\rm EL}$ and θ_0
- 4. apply inverse Momentum Exchange Method to determine u^{w} and $f_{\iota\kappa\lambda}$
- 5. apply flux boundary condition to determine $g_{L\kappa\lambda}$

Thus, the boundary condition is entirely local, with the exception of $u_{\rm EL}$ and $\theta_{\rm EL}$. Furthermore, it is defined in a linkwisemanner, and can thus be adapted to curved boundaries.

2.6 **Further Models**

225 A number of further modifications to VIRTUALFLUIDS had to be implemented in order for it to be fully equipped to conduct simulations of atmospheric boundary layers, Namely, Coriolis and buoyancy force have to be computed and a Rayleigh damping layer has to implemented.

2.6.1 Coriolis Force

The Coriolis force can be computed directly from (4) based on a user-prescribed geostrophic wind and Coriolis parameter. The Coriolis force is simply added to the body force field in our implementation. Further potential for optimization by combining 230 the computation with the collision kernel was left for future work.

2.6.2 **Buoyancy Force**

As described in the beginning, we model the effect of buoyancy via the Boussinesq approximation. After the collision kernel for q has finished, we have added a number of models to compute the buoyancy. For simplicity's sake we allocate an array with the size of the grid for a local reference temperature. The constant buoyancy provider only computes a buoyancy force according to 235 (5) and adds it to the body force field. Thus we can implement a constant reference temperature profile simply by changing the way that the reference temperature is initialized. The second variant computes buoyancy relative to the horizontally averaged temperature as is described by (5).

2.6.3 Damping Layer

240 Since the free atmosphere is essentially an undamped oscillator, spurious oscillations that can arise at the top of the capping inversion propagate throughout the domain. To mitigate these waves, it is common practice to use Rayleigh damping layers (Allaerts and Meyers, 2017). The force of in the damping layer F_D is computed by

$$F_i^{\rm D} = -f\left(\frac{z - z_{\rm s}}{z_{\rm o} - z_{\rm s}}\right) w \delta_{i3}.\tag{34}$$



250

255

265

270



The function $f(\tilde{z})$ of height normalized between start and end height $z_{\rm s}$ and $z_{\rm e}$ of the damping layer can be chosen freely in our implementation but is normally set to $f(\tilde{z}) = f_{\rm R} \sin^2 \frac{\pi}{2} \tilde{z}$ with a damping factor roughly $f_{\rm R} = 1 \times 10^{-4} 1/{\rm s}$.

2.7 Turbulence Models

As mentioned in subsection 2.1, we parameterize subgrid scale fluxes with effective viscosity and diffusivity models. A number of turbulent viscosity models were implemented for previous studies, namely the Smagorinsky (Smagorinsky, 1963), QR (Verstappen, 2011) and anisotropic minimum dissipation (AMD) model (Rozema et al., 2015). Note that due to the relation between second order cumulants and the stress tensor, the Smagorinsky and QR model can be computed very efficiently during the collision step. In addition, we have implemented a number of turbulent diffusivity models for this study, two standalone diffusivity models, namely a constant turbulent Prandtl number model and the model suggested by Moeng (1984). Finally, we have also implemented the stratified AMD model proposed by Abkar et al. (2016), which augments the original AMD model for turbulence viscosity with a term modeling the effect of buoyancy on turbulence and includes a turbulence diffusivity. As this model requires the full velocity gradient tensor, that is only available in-between collisions, we compute the effective turbulence viscosity and diffusivity for computing the collision at time step t from the velocity and temperature field at time t-1. In preliminary studies we found the stratified AMD model to yield the best results, therefore we use only this model in the remainder of this study.

3 Results

We validate our model against reference data in two stability conditions, namely conventionally neutral and stable conditions. We provide a convergence study of the advection-diffusion model in Appendix C and find the order of convergence to be slightly above two for both advection and diffusion.

3.1 Conventionally neutral boundary layer

We begin validation of our model for thermally stratified boundary layers by comparing to the conventionally neutral boundary layer (CNBL) simulation described in Berg et al. (2020). This case has also been used to validate the LES solver AMR-WIND and we have therefore two references to compare to. The domain has an extent of $2560 \,\mathrm{m} \times 2560 \,\mathrm{m} \times 896 \,\mathrm{m}$, with periodic boundaries in the streamwise and lateral direction. We conduct simulations at two resolutions, $\Delta x = 7 \,\mathrm{m}$ and $\Delta x = 3.5 \,\mathrm{m}$, corresponding to grids B and C of the original publication, respectively. At the top we employ a slip condition for momentum and the Neumann condition as described in subsection 2.4 for the potential temperature. The bottom boundary is a surface layer boundary condition with a prescribed heatflux of $0 \,\mathrm{K/ms}$ and a roughness length of $z_0 = 0.05 \,\mathrm{m}$. The geostrophic wind speed G is $5 \,\mathrm{m/s}$, the Coriolis parameter is $10^{-4} \,\mathrm{1/s}$, and the free lapse rate is $\partial \theta/\partial z = 3 \,\mathrm{K/km}$. The reference temperature is $\theta_{\mathrm{T}} = 290 \,\mathrm{K}$ and gravitational acceleration is $9.81 \,\mathrm{m/s}$. The domain is initialized with constant geostrophic wind speed and a constant temperature gradient equal to the free lapse rate. Further details of the reference case can be found in the original description. We assume an eddy turnover time $T_{\mathrm{E}} = 1700 \,\mathrm{s}$ and average from 55 to 65 T_{E} . We use the stratified AMD model



285



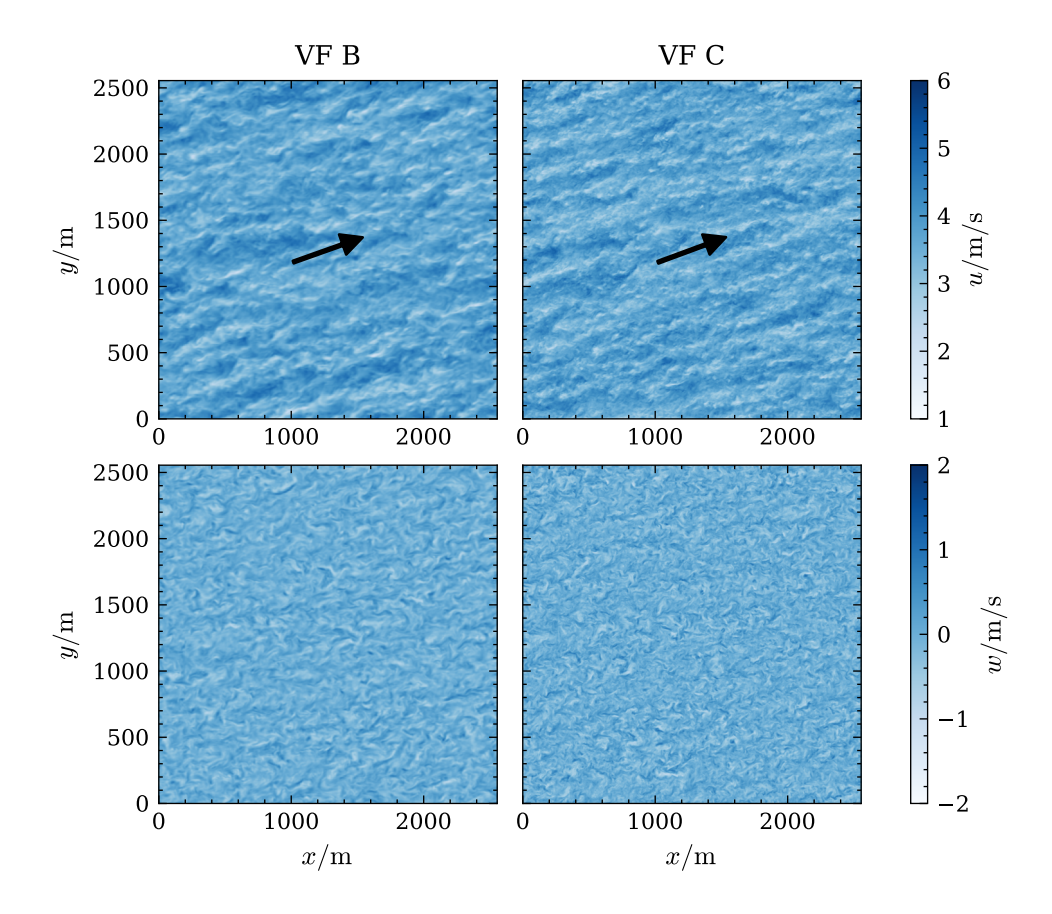


Figure 1. Instantaneous velocity fields of the CNBL case. Horizontal wind speed and vertical velocity in the plane at z = 37m shown. Black arrow indicates average wind direction in the plane.

with a model constant set to 1/3. Since we use an explicit subgrid-scale model we "turn-off" the limiter of the cumulants by setting it to 10^5 . No damping is activated.

The original study employs a pseudo-spectral code developed at the National Center for Atmospheric Research (NCAR) over the last forty years, with pseudo-spectral spatial discretization in horizontal directions and second order finite differences in the vertical direction. Time-stepping is performed with a third order Runge-Kutta scheme. In addition to the results from the original publication, we also compare to the results published in the Exawind benchmark database (Kuhn et al.) obtained with AMR-WIND. AMR-WIND utilizes a combination of finite volume and finite element methods for spatial discretization and second-order accurate time-stepping, details on AMR-WIND can be found in Kuhn et al. (2025). We compare our results to results obtained on grids C and D, with a resolution of $\Delta x = 3.5$ m and $\Delta x = 1.75$ m, respectively.

We provide a qualitative impression of the simulation in Figure 1 and Figure 2, where we show instantaneous horizontal wind speed and vertical velocity at z=35m and z=333m, equivalent to 10% and 90% of boundary layer height, respectively. Similar plots are shown in Berg et al. (2020). At the lower height we see the dominance of small scale turbulent structures in



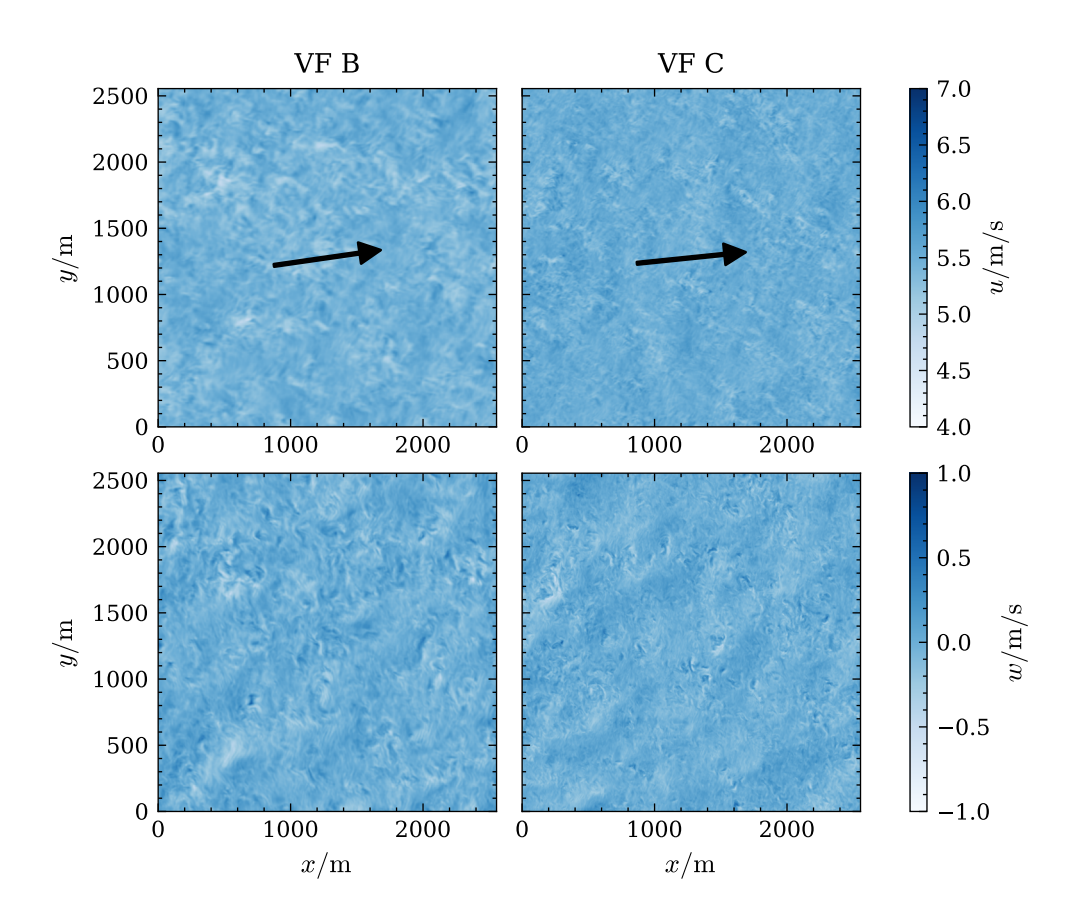


Figure 2. Instantaneous velocity fields of the CNBL case. Horizontal wind speed and vertical velocity in the plane at z = 333m shown. Black arrow indicates average wind direction in the plane.

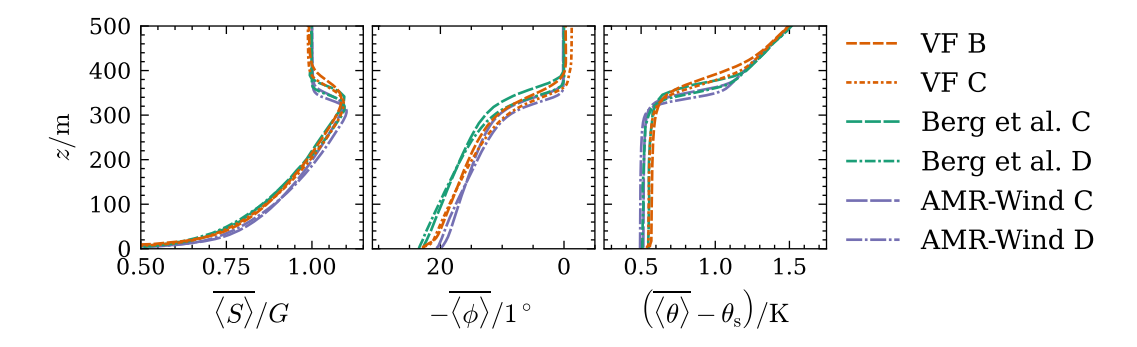


Figure 3. Vertical profiles of averaged velocity and temperature of the CNBL reference case.

both horizontal and vertical direction, as expected due to the proximity of the wall. At higher resolution we can observe that smaller scales are resolved. Close to the inversion height we find much fewer small scales, instead larger structures dominate. Comparing the direction of the mean horizontal velocity indicated by the black arrow, we observe the expected veer.



305



Table 1. Friction velocity and inversion height of the CNBL case compared to references.

	VIRTUALFLUIDS		Deig et al.		AMR-WIND	
Quantity	В	С	С	D	С	D
$u_*/\mathrm{m/s}$	0.207	0.205	0.225	0.221	0.208	0.20
$z_{ m i}/{ m m}$	381.5	362.3	372	350	352.1	337.

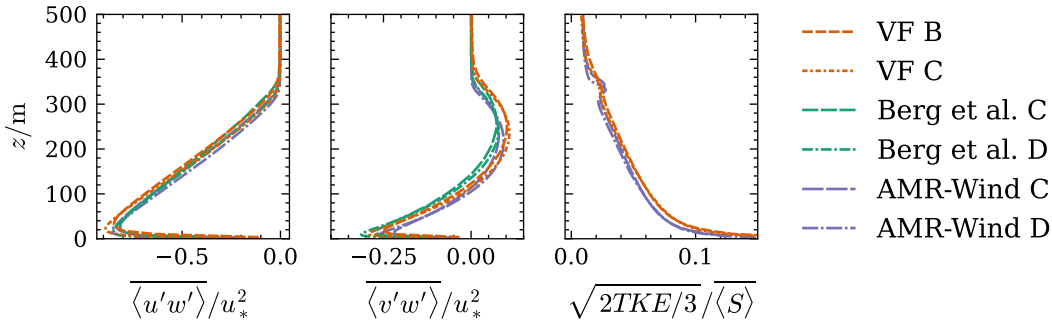


Figure 4. Vertical profiles of second order statistics of velocity and temperature of the CNBL reference case.

Moving to a more quantitative analysis, we show the horizontal averages of wind speed S, wind direction ϕ and potential temperature of our model, referred to as VF, alongside respective results from references in Figure 3. Overall, we find very good agreement between our results and the references. Especially within the boundary layer we observe very close agreement in all quantities, indicating that the boundary condition and other models behave correctly. However, we observe that the grid B is not able to properly resolve the upper edge of the capping inversion, resulting in a weaker gradient. This is in line with observations in Berg et al. (2020) and a range of other literature, for example van Heerwaarden et al. (2017). Furthermore, we observe that the wind direction in the free atmosphere is not exactly aligned with the geostrophic wind for the higher resolution case. This inaccuracy is due to the forcing of the geostrophic wind being very small compared to the streamwise velocity in the free atmosphere. Nevertheless, the error is small and seems to have a negligible effect on the wind direction below the inversion.

From the averaged results we can compute an inversion height z_i as the height with the maximum temperature gradient. We list our results next to the results reported by Berg et al. and AMR-WIND in Table 1. Furthermore, we list the friction velocity computed from the wall model. All results agree closely. The inversion height decreases with higher resolution for all solvers. AMR-WIND reports the lowest inversion heights, while our results for grid C are in the middle. We report the lowest friction velocity, while Berg et al. (2020) report the highest. Nevertheless, the results agree within 8% of each other.

We show second order statistics in Figure 4, where we present the vertical momentum flux in streamwise (u'w') and lateral direction (v'w'), and turbulence intensity based on the horizontally averaged wind speed, computed as $\sqrt{2TKE/3}/\overline{\langle S\rangle}$, where $TKE = \frac{1}{2}(\overline{\langle u'u'\rangle} + \overline{\langle v'v'\rangle} + \overline{\langle w'w'\rangle})$ is the turbulence kinetic energy. Again, we find very good agreement to both references.



315



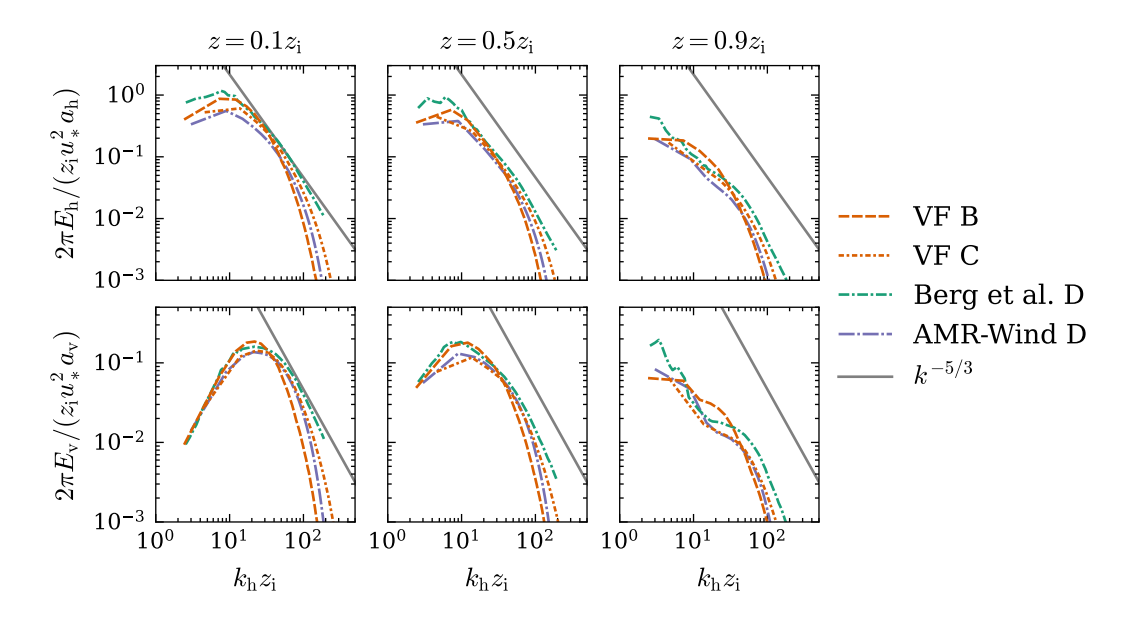


Figure 5. Horizontal (top) and vertical (bottom) spectra at z = 37m (left), z = 186m (center), and z = 333m (right).

The streamwise flux even shows excellent agreement. We can see the influence of the mismatch in wind direction in the lateral vertical momentum flux, which is slightly too high in the upper region of the boundary layer. The turbulence intensity is slightly higher near the ground than the results from AMR-WIND (there are no results presented in Berg et al. (2020)). The prominent increase of turbulence intensity at the inversion height observed in AMR-WIND is significantly less prominent in our results, even at the same resolution.

Finally, we compare spatial velocity spectra obtained at three different heights (z = 37m, 186m, 333m) in Figure 5. We compute spectra from horizontal planes following the procedure described in Berg et al. (2020). First, we compute the spectral tensors Φ_{11} , Φ_{22} and Φ_{33} from the covariance function $R_{ij}(r_x, r_y, z) = \langle u_i'(x, y, z)u_j'(x + r_x, y + r_y, z)\rangle$:

$$\Phi_{ij}(k_{x}, k_{y}, z) = \frac{1}{(2\pi)^{2}} \iint R_{ij} e^{\hat{\imath}(r_{x}k_{x} + r_{y}k_{y})} dr_{x} dr_{y},$$
(35)

where $\hat{\imath}$ is the imaginary unit. Then, we compute the ring averaged energy in horizontal and vertical spectra $E_{\rm h}(k_{\rm h})$ and $E_{\rm v}(k_{\rm h})$ with $k_{\rm h}=\sqrt{k_{\rm x}^2+k_{\rm y}^2}$:

$$E_{\rm h}(k_{\rm h}) = \frac{1}{2} \int_{0}^{2\pi} \Phi_{11}(k_{\rm h}, \phi) + \Phi_{22}(k_{\rm h}, \phi) d\phi$$
 (36)

320
$$E_{\rm v}(k_{\rm h}) = \int_{0}^{2\pi} \Phi_{33}(k_{\rm h}, \phi) \mathrm{d}\phi$$
 (37)



330

335



Results are binned into 50 equally sized bins. Wavelengths are normalized with the computed inversion height and spectra are normalized by $\frac{2\pi}{z_1u_*a_h}$ and $\frac{2\pi}{z_1u_*a_v}$ with $a_h=0.54(55/18)a$ and $a_v=0.61(55/18)a$ and a=0.5, in accordance with Berg et al. (2020). As a final step we average the spectra computed from 10 time steps to reduce noise.

Our results match the results from AMR-WIND very closely at all heights despite the lower resolution. This demonstrates the lower dissipitavity of the cumulant LBM compared to finite volume solvers. At lower wavenumbers there is also very good agreement with the results from Berg et al. (2020). At high wavenumbers, the LBM is more dissipative than the pseudospectral solver. Close to the inversion height, the small wavenumbers are lower due to the capping inversion and a characteristic hump is visible in the vertical spectra, which we could accurately reproduce with our solver.

Overall we find very good agreement in all examined quantities to the reference data, even at lower resolutions. In general, the accuracy of the model is positioned between the two reference models. The newly developed surface boundary condition is able to model the wall region accurately in neutral conditions.

Our simulations were carried out using a single NVidia RTX A6000 GPU on a workstation computer. Simulating 122500s with grid B required $3.4 \times 10^4 s$ of wall time, while the simulation of grid C ran for $5.1 \times 10^5 s$, which is approximately a 16-fold increase as is expected. Hence, we are able to run full boundary layer simulations using a workstation computer on the order of realtime. Compared to isothermal simulations on the same hardware the computational speed is reduced by around 26% due to the double distribution approach which essentially doubles the memory accessed per node as well as the additional models for Coriolis and buoyancy force. Future work will combine the different forces and collision kernels to minimize memory accesses and increase computational efficiency.

3.2 Stably stratified boundary layer

To examine the performance of our model in stable boundary layer simulations, we compare with the well-known GABLS1 benchmark (Beare et al., 2006). The domain has an extent of 400m × 400m × 400m, with periodic boundaries in the streamwise and lateral direction. The geostrophic wind is set to 8m/s and the Coriolis parameter to 1.39 × 10⁻⁴1/s. The domain is initialized with a constant velocity equal to the geostrophic wind and a two layered temperature profile. The lowest 100m are initialized with a constant temperature θ₀ = 265K, above sits an inversion layer with a temperature gradient of 0.01K/m. In the lowest 50m the temperature is superimposed with random fluctuations with amplitude 0.1K. The surface temperature is also initialized with θ₀, and a constant cooling rate of 0.25K/h is applied. The roughness length is set to z₀ = 0.1m. The reference temperature is set to 263.5 K, density is 1.3223kg/m³ and gravity to 9.81m/s². A Rayleigh damping layer is used at the top with damping factor set to 1.6 × 10⁻³1/s. We apply the same boundary conditions as in the previous case but now the surface temperature is prescribed in the surface layer boundary condition. The total simulated time is 9h and averages are computed over the last hour. We simulate two grids, one with Δx = 2m and a finer resolution of Δx = 1m.

We compare our results to data from the original benchmark and a later publication by Gadde et al. (2021). In the original paper, a number of different models are compared, with a large variety of formulations. Gadde et al. employs a pseudo-spectral discretization in horizontal directions and second order finite differences in the vertical direction and Adam-Bashforth time-stepping. They compare a three different turbulence models, the Smagorinsky model, the AMD model and the Lagrangian



365

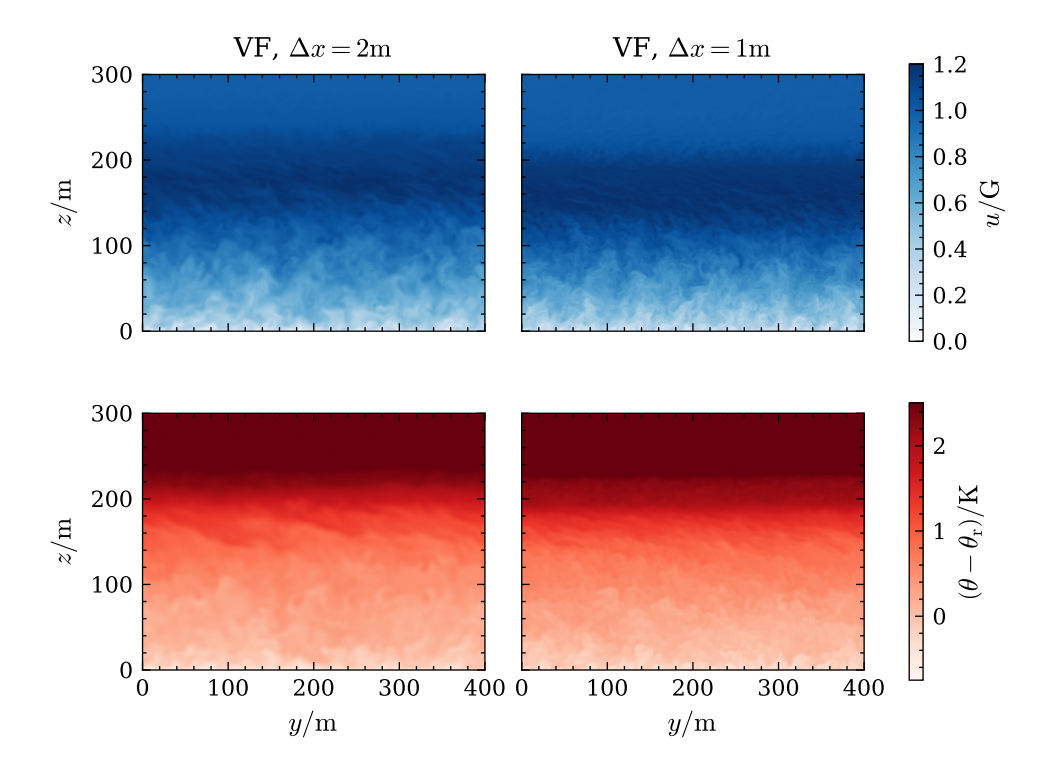


Figure 6. Instantaneous velocity and temperature fields at x = 200m of simulations of the GABLS1 reference case with both resolutions at t = 9h.

Averaged Scale Dependent model (LASD) (Bou-Zeid et al., 2005). We compare only to the results obtained with the Smagorinsky and LASD model since the results differ only marginally between LASD and AMD. Gadde et al. conduct all simulations at an isotropic resolution of 2.08m.

As with the previous case, we first show an instantaneous view of the simulation in Figure 6. The capping inversion is clearly visible in the velocity field, exhibiting a super geostrophic wind and high veer. Above the inversion a clear reduction in turbulence can be observed. At the higher resolution the transition from boundary layer to free atmosphere is sharper, which will be discussed in more detail later on. The temperature field shows a stable stratification and the presence of a strong capping inversion.

We show profiles of horizontally averaged quantities of simulating the GABLS1 reference case in Figure 7. The wind speed below the inversion agrees well with the reference data in both cases. The case with lower resolution exhibits a significantly lower velocity gradient than the higher resolution case. This is in line with findings from Beare et al. (2006), where simulations at a lower resolution also exhibited this behavior. At the higher resolution, our results match those of Gadde et al. (2021) closely. We find higher negative veer in the inversion layer compared to Gadde et al., particularly at higher resolution, which also results in higher wind speed in that region. However, there seems to be only a very limited effect on the flow in the boundary layer. The temperature profile at the lower resolution agrees well with the reference data within the boundary layer.



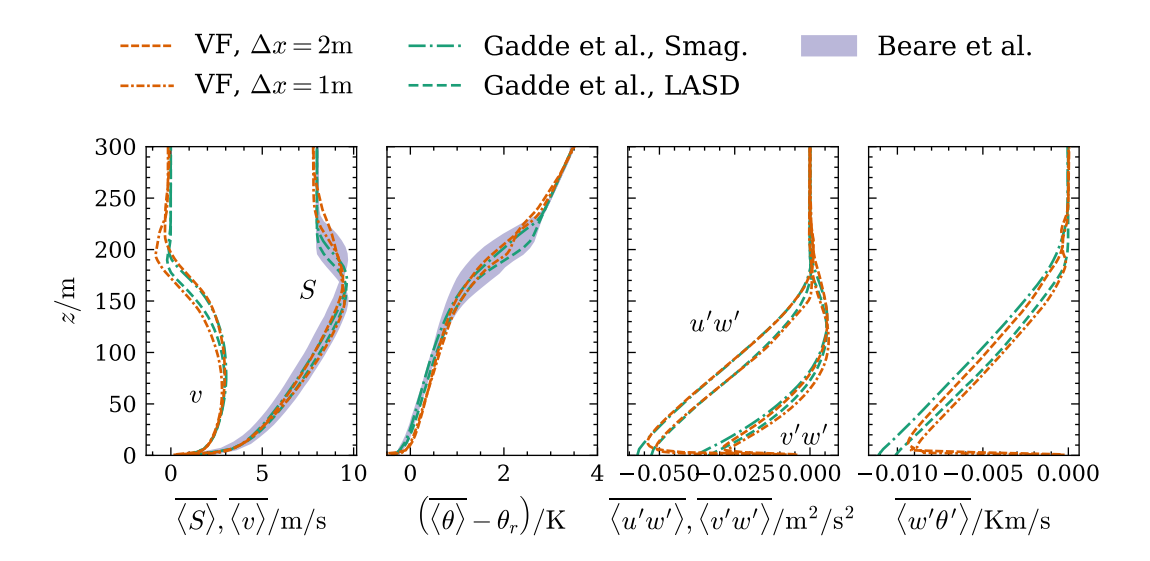


Figure 7. Planar average first and second order statistics of the GABLS1 reference case. From left to right: Wind speed and lateral velocity; temperature; momentum fluxes; and vertical temperature flux. The area covered by all results at resolution 2m from (Beare et al., 2006) are shown as blue shaded area.

Table 2. Friction velocity, boundary layer height, and buoyancy flux of the GABLS1 case.

	VIRTUALFLUIDS		Beare	Gadde et al.		
Quantity	$\Delta x = 2\mathrm{m}$	$\Delta x = 1 \mathrm{m}$	$\Delta x = 2\mathrm{m}$	$\Delta x = 1 \mathrm{m}$	Smag.	LASD
$u_*/\mathrm{m/s}$	0.27	0.26	0.24 - 0.28	_	0.265	0.253
h/m	180	159	162 - 197	149 – 164	166	166
$-\frac{g\langle w\theta\rangle}{\theta_0}\cdot 10^4/\text{m}^2/\text{s}^3$	3.86	3.44	3.5 - 4.7	_	4.1	3.8

In the inversion layer the gradient is slightly lower than that of Gadde et al. (2021), but still well within the range of results from Beare et al. (2006). At the higher resolution we find very good agreement. The vertical momentum fluxes agree very well with the reference results. Only results from Gadde et al. (2021) are available. The vertical temperature fluxes give a similar picture, although they are slightly smaller than the reference data. Furthermore, there exists a small hump in the results from the case with lower resolution. We believe this is connected to the velocity profile, where the top of the inversion had a significantly lower gradient.

A comparison of some quantities of interest is shown in Table 2. Note that the friction velocity and buoyancy flux are computed from the total fluxes at the second node since this is the node we use as exchange location for the wall model. We compute the boundary layer height h with the same method used in the references. We first find the height $h_{0.05}$ at which the shear stress $\sqrt{(u'w')^2 + (v'w')^2}$ is less than 5% of the wall shear stress and extrapolate by $h = \frac{h_{0.05}}{0.95}$.



390

395



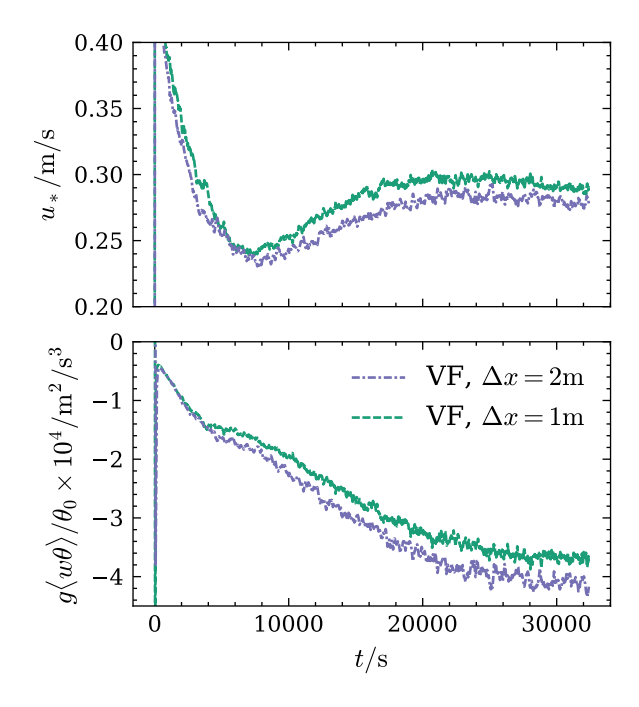


Figure 8. Time evolution of friction velocity and buoyancy flux of the GABLS1 reference case.

The friction velocity and buoyancy flux are well within the range of the reference results. This indicates that our wall modeling approach and boundary condition yield accurate results. The boundary layer height decreases with increasing resolution as was also observed in Beare et al. (2006).

To examine the performance of the new boundary condition in more detail, we show the time evolution of friction velocity and buoyancy flux in Figure 8. In the initial seconds of the simulation, both quantities exhibit large spikes. The friction velocity first decreases quickly as a boundary layer develops, decreasing shear in the lowest part of the domain. The surface heat flux increases in magnitude as the surface cools and thus the temperature gradient near the surface increases. Both quantities stabilize towards the end of the simulation, indicating that the simulation has reached a state of equilibrium. This behavior is qualitatively similar to the results reported in Beare et al. (2006) and Sauer and Muñoz-Esparza (2020). Despite varying formulations, different approaches yield similar results near the equilibrium state of the boundary layer.

It is worth noting that the reference results also yield a large variation in all observed quantities, as noted by other studies comparing to this case, e.g. van Heerwaarden et al. (2017) and Sauer and Muñoz-Esparza (2020). Generally, our results within the boundary layer fall well within the range of the results obtained by other solvers, despite the differences in approach, subgrid-scale models, etc. At the top of the boundary layer our model requires higher resolution than most other solvers to accurately represent the capping inversion. We believe this is caused by the model not representing the temperature gradient accurately enough. One way to improve the model is to further refine the collision operator of the advection diffusion LBM. In a comparison of different advection diffusion collision operators, Gruszczyński and Łaniewski-Wołłk (2022) found a two-





relaxation time central moment operator to be more accurate than the central moment operator most similar to the one employed here. By introducing more relaxation times, leading order error terms can be canceled out and accuracy of the collision operator can be improved, as was done, for example, in Geier et al. (2017).

400 4 Conclusions

405

420

425

This paper presents a novel method for conducting large eddy simulation of thermally stratified atmospheric boundary layers using the double-distribution function (DDF) lattice Boltzmann method (LBM) in a GPU-resident solver. Very few applications of the LBM to stratified atmospheric boundary layers have been presented in the literature so far and this work comprises the first application of a DDF approach to such flows in conjunction with employing GPUs. We give a thorough description of our methodology for the simulation of the bulk flow, present a novel boundary condition to use a combined wall model for wall shear stress and heat flux prescribed by Monin-Obukhov similarity theory and present other models implemented in the GPU-resident LBM solver VIRTUALFLUIDS in order to simulate stratified atmospheric boundary layers, including horizontally averaged buoyancy, Coriolis force and Rayleigh damping layer.

We test our model in simulations of conventionally neutral and stably stratified boundary layers. Simulations of the conventionally neutral boundary layer agree very well with reference data obtained both with pseudo-spectral and finite volume methods. At a coarse resolution of 7m, the inversion layer can not be represented accurately. At a finer resolution of 3.5m the results match closely with the reference data at twice the resolution obtained with pseudo-spectral and finite volume methods. Second order statistics also agree very well. The spectra obtained at three heights show that the LBM exhibits excellent spectral properties and has lower diffusion than the finite volume solver at higher resolution. Damping of vertical motions near the inversion layer is also clearly present.

Simulations of the stably stratified GABLS1 reference case also yield satisfactory results. The proposed boundary condition is able to properly reproduce the friction velocity and buoyancy flux at the wall. The boundary layer height agrees with results obtained at the same resolution.

A general shortcoming of the model is its inability to correctly reproduce the direction of the geostrophic wind and this discrepancy grows with increasing resolution. However, we find that this does not affect the results in the boundary layer and the misalignment is small. Overall we achieve satisfactory accuracy for both cases. The method exhibits the expected behavior, being in general more accurate than a second order finite volume method, but not as accurate as a pseudo-spectral approach.

The present model exhibits excellent computational efficiency. All simulations, even the highly resolved neutral boundary layer with ≈ 140 million nodes, are carried out on a single graphics card. At a coarse resolution of $\Delta x = 7 \mathrm{m}$, the simulation is carried out four times faster than realtime. Increasing resolution to $\Delta x = 3.5 \mathrm{m}$ results in a simulation at 0.25 realtime.

This article comprises a model for an empty boundary layer with flat terrain. Future work will focus on implementing a precursor-successor setup to simulate wind farms. One of the limitations of our model is that the surface layer boundary condition is only formulated for straight walls. As noted by Asmuth et al. (2021), an extension of the inverse Momentum Exchange Method is possible but not available as of yet. Nevertheless this work represents an important step for the lattice Boltzmann





method and CFD in general towards simulations of stratified boundary layers while fully leveraging the computational efficiency of GPUs. It represents one of the most cost-effective and fastest methods available to conduct LES of such complexity. The reduction in computational cost benefits researchers in many ways, from reducing development time to enabling larger parameter studies. Furthermore, a reduction in computational cost is crucial for enabling industrial application of LES, for example in the wind energy sector. That way, manufacturers, developers and operators can take into account the complex behavior of the atmospheric boundary layer and reduce model uncertainties, ultimately reducing the cost of electricity.

Code and data availability. VIRTUALFLUIDS is available open source at https://git.rz.tu-bs.de/irmb/VirtualFluids. The model described in this paper is published in version 1.3. The data for creating the plots in section 3 and the corresponding postprocessing scripts are available at https://source.coderefinery.org/wind_energy_uu/stratificationinlbm

Appendix A: Unsuccessful preliminary studies

The development of this model was rich with paths that lead us nowhere, as is often the case when developing a new model. We want to record some of those paths in the hope that others might learn to either avoid those paths or will see where we went wrong and will be able to tell us what we should have done instead.

A1 Hybrid Finite Difference Scheme

We first tried to implement a hybrid solver by using finite differences for the advection-diffusion problem. The hybrid method has a number of benefits. The finite differences approach is much simpler and much more well known, hence there is also more 445 literature on the topic. Furthermore, it requires significantly less memory while also yielding higher computational performance. Hence it is used in a number of other thermal LBM models, for example Onodera et al. (2021) and (Feng et al., 2021). Results for the canonical test cases looked very promising so we decided to pursue this direction further. However, when we simulated the atmospheric boundary layer we could never avoid spurious oscillations that ultimately degraded the simulation, particularly at the top of the inversion layer. We implemented a variety of approaches, beginning with central differences and 450 Euler forward time-stepping. We refined our approach, using a variety of different finite difference schemes, such as second order upwind, the MUSCL scheme, QUICK and QUICKEST scheme and mixed fourth order central differences and QUICK scheme. We also tried a second order Adam-Bashforth time integration, but all to no avail. At this point we pivoted to a DDF approach that was already implemented in VIRTUALFLUIDS since adding even higher order approaches seemed not promising. As of yet it is unclear, what were the differences in our approach to, for example the model implemented in PROLB (Feng 455 et al., 2021). On the one hand, we use a much less diffusive collision operator, thus oscillations are not damped as much. On the other hand, no other study actually simulates a capping inversion, where the oscillations originated in our simulations. Furthermore, there is very little literature concerning this issue. We speculate that the instabilities occur due to the differences in stencil / lattice. The lattice Boltzmann method only access the direct neighbors, while all the higher order methods require





460 information from the second neighbor as well, thus information can travel at different speeds. As this was not the aim of this work, we did not explore this direction further.

A2 Reference temperature

To improve the numerical precision of the populations $g_{\iota\kappa\lambda}$ are set so that $\theta - \theta_{\rm m} = \sum g_{\iota\kappa\lambda}$. The choice of the reference temperature $\theta_{\rm m}$ is crucial to improve the accuracy of the simulation. A naïve choice would be to either set it to the reference temperature $\theta_{\rm r}$ or the surface temperature $\theta_{\rm 0}$, however we found that oscillations tended to originate from areas where the temperature is far away from $\theta_{\rm m}$. We found that the best choice was usually to set $\theta_{\rm m}$ to a value of the temperature in the inversion layer.

Appendix B: Boundary Conditions Fluid

We set a slip boundary condition by a similar method as we set the flux boundary condition. At the upper most fluid node we 470 compute the velocity from (7) and then compute the tangential velocity with

$$u_i^t = u_i - (u_i n_i) n_i. ag{B1}$$

Then we apply the bounce back rule:

$$f_{\iota\kappa\lambda} = f_{\iota\kappa\lambda} - 2\rho w_{\iota\kappa\lambda} \frac{u_i c_{\iota\kappa\lambda,i}}{c_s^2}.$$
 (B2)

At the bottom boundary we employ the iMEM approach from Asmuth et al. (2021). We want to give a few clarifications and correct some misprints in the original publication. Recall that the momentum transferred from *the fluid to the wall* is

$$\Delta p_{\iota\kappa\lambda,i} = \left(f_{\iota\kappa\lambda} + f_{\overline{\iota\kappa\lambda}} \right) c_{\iota\kappa\lambda,i}. \tag{B3}$$

Hence, the total force exerted onto the wall by the fluid is

$$F_i = \frac{\Delta x^3}{\Delta t} \sum_{i \in \lambda \in \Gamma} \Delta p_{\iota \kappa \lambda, i}, \tag{B4}$$

where Γ is the set of all links cutting the wall. From the wall model we compute the force acting on the wall from the wall shear stress

$$F_i = \tau_i^{\mathrm{w}} \Delta x^2$$
. (B5)

We now seek a wall velocity u^w , such that the bounce back rule (B2) results in the correct force. To that end, we split the force into two components, the force due to the population and due to the wall velocity, F^f and F^{u_w} :

$$F_i^{f} = \frac{\Delta x^3}{\Delta t} \sum_{\iota \kappa \lambda \in \Gamma} c_{\iota \kappa \lambda, i} \left(f_{\iota \kappa \lambda} + f_{\overline{\iota \kappa \lambda}} \right)$$
 (B6)

485
$$F_i^{u_{\rm w}} = -\frac{\Delta x^3}{\Delta t} \sum_{\iota \kappa \lambda \in \Gamma} 2\rho w_{\iota \kappa \lambda} c_{\iota \kappa \lambda, i} \frac{u_j c_{\iota \kappa \lambda, j}}{c_{\rm s}^2}.$$
 (B7)





Thus, $F_i^{u_w} = F_i - F_i^f$, resulting in a system of equations that needs to be solved for u^w . For the case of a straight wall at the bottom, the solution is

$$\boldsymbol{u}^{\text{W}} = -\frac{3c_{\text{s}}^2}{\rho} \frac{\Delta t^2}{\Delta x^4} (3F_1^{u_{\text{w}}}, 3F_2^{u_{\text{w}}}, F_3^{u_{\text{w}}})^T.$$
(B8)

Appendix C: Converge study

To determine the order of convergence of the advection diffusion equation numerically, we simulate the advection diffusion of a Gaussian Hill of concentration. Note, that in this case, θ is a passive scalar. The initial field of concentration θ is described by (Krüger et al., 2017, p. 322)

$$\theta(\boldsymbol{x}, t = 0) = \theta_0 \exp\left(-\frac{|\boldsymbol{x} - \boldsymbol{x}_0|^2}{2\sigma_0}\right). \tag{C1}$$

Under a constant advection velocity u,

495
$$\theta(\boldsymbol{x},t) = \frac{\sigma_0^2}{\sigma_0^2 + \sigma_D^2} \theta_0 \exp{-\frac{|\boldsymbol{x} - \boldsymbol{x}_0 - \boldsymbol{u}t|^2}{2(\sigma_0^2 + \sigma_D^2)}}$$
 (C2)

is a solution for the advection-diffusion equation

$$\frac{\partial \theta}{\partial t} + \boldsymbol{u} \cdot \frac{\partial \theta}{\partial \boldsymbol{x}} = \frac{1}{\text{Pe}} \frac{\partial^2 \theta}{\partial \boldsymbol{x}^2},\tag{C3}$$

with $\sigma_D = \sqrt{2Dt}$, the Peclét Number $\text{Pe} = \frac{\sigma_0 U}{D}$ and $u = [1,1,1]^T U$. We conduct a convergence study for a diffusion dominated problem (Pe = 1) and an advection dominated problem ($\text{Pe} = 10^5$). We vary $N = \sigma_0/\Delta x = 2,4,8,16$, while we keep $\sigma_0 = 1$ and $\Delta t = 1$ constant. In case of Pe = 1, we set the diffusivity in lattice units $\tilde{D} = D \frac{\Delta t}{\Delta x^2} = 0.01$ and we simulate until $T_{\text{end}} = 0.3 \frac{\sigma_0}{U}$ is reached. In the case of $\text{Pe} = 10^5$, $\tilde{D} = 1 \times 10^{-5}$, and $T_{\text{end}} = 3 \frac{\sigma_0}{U}$. In both cases the domain has a size of $18\sigma_0 \times 18\sigma_0 \times 18\sigma_0$. To optimally utilize the simulation domain we set $x_0 = -T_{\text{end}}U/2$. The analytical solutions for both Peclét numbers at t = 0 and $t = T_{\text{end}}$ is shown in Figure C1. The results of the convergence test for both Peclét numbers can be found in Figure C2. The results clearly show a convergence rate slightly above second order in both cases, as expected. More precisely, we compute a convergence rate of 2.5 and 2.2 for Pe = 1 and $\text{Pe} = 10^5$, respectively. A more detailed view of the error can be found in Figure C3, where we show the absolute difference between analytical and numerical solution. We see that in both cases errors decrease with higher resolution and that the error is symmetric in the diffusion dominated case, while advection case exhibits errors aligned with the direction of advection. We also see that errors become negligibly small towards the boundaries of the domain, so the domain was chosen large enough to not affect the results.

Author contributions. HK, HA and SI conceptualized the project. HK, HA, MG and MS developed the methodology and implemented the code. HK conducted the simulations and the postprocessing under guidance of HA and SI. HK prepared the original draft, all authors reviewed and edited the manuscript. SI acquired the resources and supervised the project.



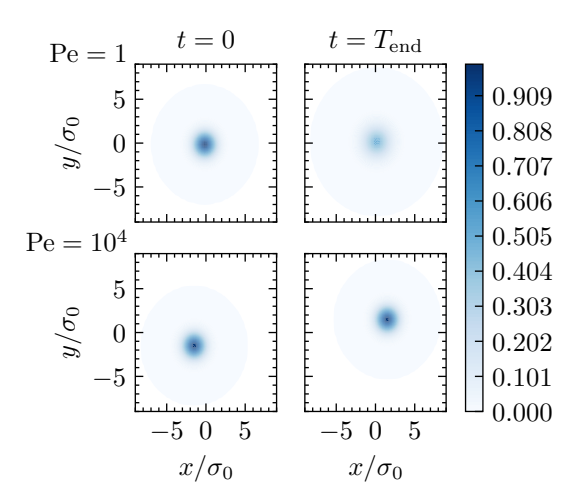


Figure C1. Analytical solution for the concentration in the test case of a Gaussian hill of concentration, projected onto the x-y plane. In the white region concentration $\theta \le 1 \times 10^{-10}$

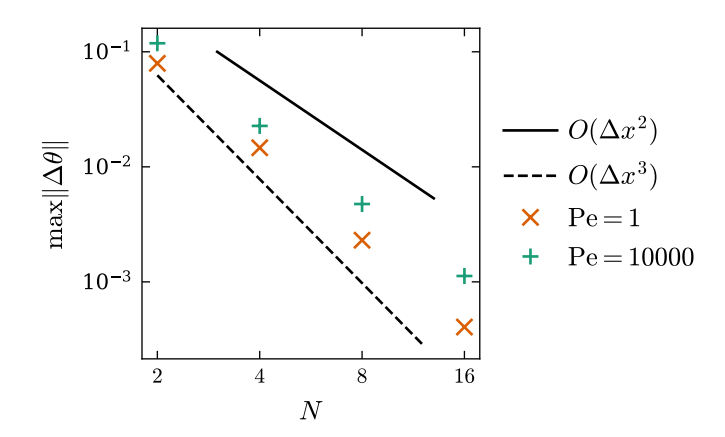


Figure C2. Maximum error $\Delta\theta$ of the numerical results of simulating the advection-diffusion of a Gaussian hill of concentration.



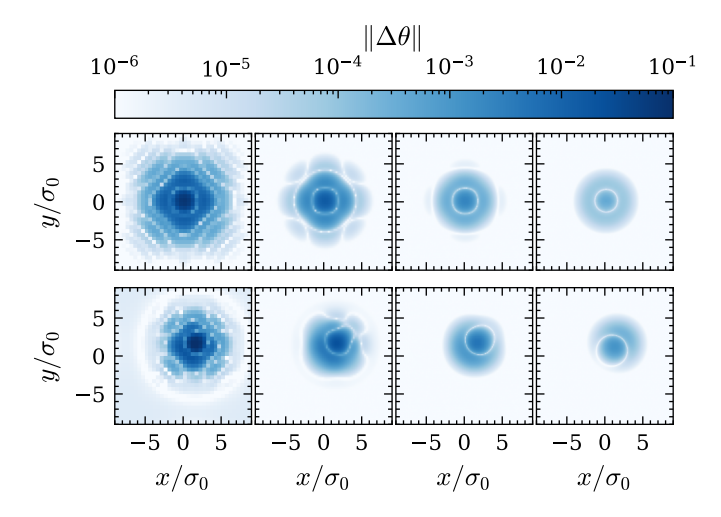


Figure C3. Absolute difference between analytical and numerical solution of the Gaussian hill of concentration at $t = T_{end}$. Top row shows the case with Pe = 1, bottom row the case with $Pe = 10^4$. Resolution increases from left to right.

Competing interests. The authors declare no competing interests.

Acknowledgements. HK would like to thank Antonio Salvini, Luca Lanzilao, and Hugo Olivares-Espinosa for their helpful discussions and Lawrence Cheung and Gopal Yalla for help with the results from the Exawind benchmark.





References

535

- Abkar, M., Bae, H. J., and Moin, P.: Minimum-Dissipation Scalar Transport Model for Large-Eddy Simulation of Turbulent Flows, Physical Review Fluids, 1, 041701, https://doi.org/10.1103/PhysRevFluids.1.041701, https://link.aps.org/doi/10.1103/PhysRevFluids.1.041701, 2016.
- Alihussein, H., Geier, M., and Krafczyk, M.: A Parallel Coupled Lattice Boltzmann-Volume of Fluid Framework for Modeling Porous Media Evolution, Materials, 14, 2510, https://doi.org/10.3390/ma14102510, https://www.mdpi.com/1996-1944/14/10/2510, 2021.
 - Allaerts, D. and Meyers, J.: Boundary-Layer Development and Gravity Waves in Conventionally Neutral Wind Farms, Journal of Fluid Mechanics, 814, 95–130, https://doi.org/10.1017/jfm.2017.11, https://www.cambridge.org/core/product/identifier/S0022112017000118/type/journal_article, 2017.
- Arya, S. P.: Introduction to Micrometeorology, vol. 79 of *International Geophysics Series*, Academic Press, San Diego, 2nd edn., ISBN 978-0-12-059354-5, 2001.
 - Asmuth, H., Janßen, C. F., Olivares-Espinosa, H., and Ivanell, S.: Wall-Modeled Lattice Boltzmann Large-Eddy Simulation of Neutral Atmospheric Boundary Layers, Physics of Fluids, 33, 105 111, https://doi.org/10.1063/5.0065701, https://aip.scitation.org/doi/10.1063/5. 0065701, 2021.
- Basu, S., Holtslag, A. A. M., Van De Wiel, B. J. H., Moene, A. F., and Steeneveld, G.-J.: An Inconvenient "Truth" about Using Sensible Heat Flux as a Surface Boundary Condition in Models under Stably Stratified Regimes, Acta Geophysica, 56, 88–99, https://doi.org/10.2478/s11600-007-0038-y, http://link.springer.com/10.2478/s11600-007-0038-y, 2008.
 - Beare, R. J., Macvean, M. K., Holtslag, A. A. M., Cuxart, J., Esau, I., Golaz, J.-C., Jimenez, M. A., Khairoutdinov, M., Kosovic, B., Lewellen, D., Lund, T. S., Lundquist, J. K., Mccabe, A., Moene, A. F., Noh, Y., Raasch, S., and Sullivan, P.: An Intercomparison of Large-Eddy Simulations of the Stable Boundary Layer, Boundary-Layer Meteorology, 118, 247–272, https://doi.org/10.1007/s10546-004-2820-6, https://doi.org/10.1007/s10546-004-2820-6, 2006.
 - Berg, J., Patton, E. G., and Sullivan, P. P.: Large-Eddy Simulation of Conditionally Neutral Boundary Layers: A Mesh Resolution Sensitivity Study, Journal of the Atmospheric Sciences, 77, 1969–1991, https://doi.org/10.1175/JAS-D-19-0252.1, https://journals.ametsoc.org/view/journals/atsc/77/6/JAS-D-19-0252.1.xml, 2020.
- Bou-Zeid, E., Meneveau, C., and Parlange, M.: A Scale-Dependent Lagrangian Dynamic Model for Large Eddy Simulation of Complex Turbulent Flows, Physics of Fluids, 17, 025 105, https://doi.org/10.1063/1.1839152, https://aip.scitation.org/doi/full/10.1063/1.1839152, 2005.
 - Businger, J. A., Wyngaard, J. C., Izumi, Y., and Bradley, E. F.: Flux-Profile Relationships in the Atmospheric Surface Layer, Journal of the Atmospheric Sciences, 28, 181–189, https://doi.org/10.1175/1520-0469(1971)028<0181:FPRITA>2.0.CO;2, https://journals.ametsoc.org/view/journals/atsc/28/2/1520-0469_1971_028_0181_fprita_2_0_co_2.xml, 1971.
 - d'Humières, D.: Generalized Lattice-Boltzmann Equations, in: Rarefied Gas Dynamics: Theory and Simulations, Progress in Astronautics and Aeronautics, pp. 450–458, American Institute of Aeronautics and Astronautics, ISBN 978-1-56347-080-6, https://arc.aiaa.org/doi/10. 2514/5.9781600866319.0450.0458, 1994.
- Feng, Y., Miranda-Fuentes, J., Guo, S., Jacob, J., and Sagaut, P.: ProLB: A Lattice Boltzmann Solver of Large-Eddy Simulation for Atmospheric Boundary Layer Flows, Journal of Advances in Modeling Earth Systems, 13, e2020MS002107, https://doi.org/10.1029/2020MS002107, https://agupubs.onlinelibrary.wiley.com/doi/abs/10.1029/2020MS002107, 2021.





- Gadde, S. N., Stieren, A., and Stevens, R. J. A. M.: Large-Eddy Simulations of Stratified Atmospheric Boundary Layers: Comparison of Different Subgrid Models, Boundary-Layer Meteorology, 178, 363–382, https://doi.org/10.1007/s10546-020-00570-5, https://doi.org/10.1007/s10546-020-00570-5, 2021.
- Gehrke, M. and Rung, T.: Periodic Hill Flow Simulations with a Parameterized Cumulant Lattice Boltzmann Method, International Journal for Numerical Methods in Fluids, 94, 1111–1154, https://doi.org/10.1002/fld.5085, https://onlinelibrary.wiley.com/doi/abs/10.1002/fld.5085, 2022.
 - Geier, M., Schönherr, M., Pasquali, A., and Krafczyk, M.: The Cumulant Lattice Boltzmann Equation in Three Dimensions: Theory and Validation, Computers & Mathematics with Applications, 70, 507–547, https://doi.org/10.1016/j.camwa.2015.05.001, https://linkinghub.elsevier.com/retrieve/pii/S0898122115002126, 2015.
 - Geier, M., Pasquali, A., and Schönherr, M.: Parametrization of the Cumulant Lattice Boltzmann Method for Fourth Order Accurate Diffusion Part I: Derivation and Validation, Journal of Computational Physics, 348, 862–888, https://doi.org/10.1016/j.jcp.2017.05.040, https://linkinghub.elsevier.com/retrieve/pii/S0021999117304230, 2017.
- Geier, M., Lenz, S., Schönherr, M., and Krafczyk, M.: Under-Resolved and Large Eddy Simulations of a Decaying Taylor–Green Vortex with
 the Cumulant Lattice Boltzmann Method, Theoretical and Computational Fluid Dynamics, https://doi.org/10.1007/s00162-020-00555-7,
 https://doi.org/10.1007/s00162-020-00555-7, 2020.
 - Geier, M., Kutscher, K., Schönherr, M., Wellmann, A., Peters, S., Alihussein, H., Linxweiler, J., and Krafczyk, M.: VirtualFluids Open Source Parallel LBM Solver, Computer Physics Communications, p. 109810, https://doi.org/10.1016/j.cpc.2025.109810, https://www.sciencedirect.com/science/article/pii/S0010465525003121, 2025.
- Gruszczyński, G. and Łaniewski-Wołłk, Ł.: A Comparative Study of 3D Cumulant and Central Moments Lattice Boltzmann Schemes with Interpolated Boundary Conditions for the Simulation of Thermal Flows in High Prandtl Number Regime, International Journal of Heat and Mass Transfer, 197, 123 259, https://doi.org/10.1016/j.ijheatmasstransfer.2022.123259, https://www.sciencedirect.com/science/article/pii/ S0017931022007293, 2022.
- Jacob, J., Malaspinas, O., and Sagaut, P.: A New Hybrid Recursive Regularised Bhatnagar–Gross–Krook Collision Model for Lattice Boltz-575 mann Method-Based Large Eddy Simulation, Journal of Turbulence, 19, 1051–1076, https://doi.org/10.1080/14685248.2018.1540879, https://doi.org/10.1080/14685248.2018.1540879, 2018.
 - King, M.-F., Khan, A., Delbosc, N., Gough, H. L., Halios, C., Barlow, J. F., and Noakes, C. J.: Modelling Urban Airflow and Natural Ventilation Using a GPU-based Lattice-Boltzmann Method, Building and Environment, 125, 273–284, https://doi.org/10.1016/j.buildenv.2017.08.048, https://www.sciencedirect.com/science/article/pii/S036013231730402X, 2017.
- 580 Krüger, T., Kusumaatmaja, H., Kuzmin, A., Shardt, O., Silva, G., and Viggen, E. M.: The Lattice Boltzmann Method: Principles and Practice, Graduate Texts in Physics, Springer International Publishing, 1 edn., ISBN 978-3-319-44647-9, http://link.springer.com/10.1007/978-3-319-44649-3, 2017.
 - Kuhn, M. B., Cheung, L., Yalla, G., Henry de Frahan, M. T., and Mohan, P.: Exawind Benchmarks, https://github.com/Exawind/exawind-benchmarks/tree/main/amr-wind/atmospheric_boundary_layer/neutral, accessed 2025-09-16.
- Kuhn, M. B., Henry de Frahan, M. T., Mohan, P., Deskos, G., Churchfield, M., Cheung, L., Sharma, A., Almgren, A., Ananthan, S., Brazell, M. J., Martínez-Tossas, L. A., Thedin, R., Rood, J., Sakievich, P., Vijayakumar, G., Zhang, W., and Sprague, M.: AMR-Wind: A Performance-Portable, High-Fidelity Flow Solver for Wind Farm Simulations, Wind Energy, 28, e70010, https://doi.org/10.1002/we.70010, https://onlinelibrary.wiley.com/doi/abs/10.1002/we.70010, 2025.



600



- Lanzilao, L. and Meyers, J.: Effects of Self-Induced Gravity Waves on Finite Wind-Farm Operations Using a Large-Eddy Simulation Framework, Journal of Physics: Conference Series, 2265, 022 043, https://doi.org/10.1088/1742-6596/2265/2/022043, https://doi.org/10.1088/1742-6596/2265/2/022043, 2022.
 - Lanzilao, L. and Meyers, J.: Parametric Large-Eddy Simulation Study of Wind-Farm Blockage and Waves Conventionally Neutral Boundary Lavers. Journal of Fluid Mechanics. 979. A54. https://doi.org/10.1017/jfm.2023.1088, https://www.cambridge.org/core/journals/journal-of-fluid-mechanics/article/
- parametric-largeeddy-simulation-study-of-windfarm-blockage-and-gravity-waves-in-conventionally-neutral-boundary-layers/0BE3E25A18D2583FB4E8E12BA0ABC8AC, 2024.
 - Lenz, S., Schönherr, M., Geier, M., Krafczyk, M., Pasquali, A., Christen, A., and Giometto, M.: Towards Real-Time Simulation of Turbulent Air Flow over a Resolved Urban Canopy Using the Cumulant Lattice Boltzmann Method on a GPGPU, Journal of Wind Engineering and Industrial Aerodynamics, 189, 151–162, https://doi.org/10.1016/j.jweia.2019.03.012, https://www.sciencedirect.com/science/article/pii/S0167610518309528, 2019.
 - Malaspinas, O. and Sagaut, P.: Wall Model for Large-Eddy Simulation Based on the Lattice Boltzmann Method, Journal of Computational Physics, 275, 25–40, https://doi.org/10.1016/j.jcp.2014.06.020, https://linkinghub.elsevier.com/retrieve/pii/S0021999114004276, 2014.
 - Moeng, C.-H.: A Large-Eddy-Simulation Model for the Study of Planetary Boundary-Layer Turbulence, Journal of the Atmospheric Sciences, 41, 2052–2062, https://doi.org/10.1175/1520-0469(1984)041<2052:ALESMF>2.0.CO;2, https://journals.ametsoc.org/view/journals/atsc/41/13/1520-0469_1984_041_2052_alesmf_2_0_co_2.xml, 1984.
 - Obrecht, C., Kuznik, F., Tourancheau, B., and Roux, J.-J.: The TheLMA Project: A Thermal Lattice Boltzmann Solver for the GPU, Computers & Fluids, 54, 118–126, https://doi.org/10.1016/j.compfluid.2011.10.011, http://www.sciencedirect.com/science/article/pii/S0045793011003100, 2012.
- Obrecht, C., Kuznik, F., Tourancheau, B., and Roux, J.-J.: Multi-GPU Implementation of a Hybrid Thermal Lattice Boltzmann Solver Using the TheLMA Framework, Computers & Fluids, 80, 269–275, https://doi.org/10.1016/j.compfluid.2012.02.014, http://www.sciencedirect.com/science/article/pii/S0045793012000680, 2013.
 - Obrecht, C., Kuznik, F., Merlier, L., Roux, J.-J., and Tourancheau, B.: Towards Aeraulic Simulations at Urban Scale Using the Lattice Boltzmann Method, Environmental Fluid Mechanics, 15, 753–770, https://doi.org/10.1007/s10652-014-9381-0, https://doi.org/10.1007/s10652-014-9381-0, 2015.
- Onodera, N., Aoki, T., Shimokawabe, T., and Kobayashi, H.: Large-Scale LES Wind Simulation Using Lattice Boltzmann Method for a 10 Km x 10 Km Area in Metropolitan Tokyo, TSUBAME ESJ, 9, 2013.
 - Onodera, N., Idomura, Y., Hasegawa, Y., Nakayama, H., Shimokawabe, T., and Aoki, T.: Real-Time Tracer Dispersion Simulations in Oklahoma City Using the Locally Mesh-Refined Lattice Boltzmann Method, Boundary-Layer Meteorology, https://doi.org/10.1007/s10546-020-00594-x, https://doi.org/10.1007/s10546-020-00594-x, 2021.
- 620 Ørsted: Ørsted Presents Update on Its Long-Term Financial Targets, https://ml-eu.globenewswire.com/Resource/Download/b0e11bc9-bd4a-4bfe-a91c-e99b7c5cd7a2, 2019.
 - Rozema, W., Bae, H. J., Moin, P., and Verstappen, R.: Minimum-Dissipation Models for Large-Eddy Simulation, Physics of Fluids, 27, 085 107, https://doi.org/10.1063/1.4928700, https://doi.org/
- Sauer, J. A. and Muñoz-Esparza, D.: The FastEddy® Resident-GPU Accelerated Large-Eddy Simulation Framework: Model Formulation, Dynamical-Core Validation and Performance Benchmarks, Journal of Advances in Modeling Earth Systems, 12, e2020MS002100, https://doi.org/10.1029/2020MS002100, https://onlinelibrary.wiley.com/doi/abs/10.1029/2020MS002100, 2020.





- Smagorinsky, J.: GENERAL CIRCULATION EXPERIMENTS WITH THE PRIMITIVE EQUATIONS: I. THE BASIC EXPERIMENT, Monthly Weather Review, 91, 99–164, https://doi.org/10.1175/1520-0493(1963)091<0099:GCEWTP>2.3.CO;2, https://journals.ametsoc.org/view/journals/mwre/91/3/1520-0493_1963_091_0099_gcewtp_2_3_co_2.xml, 1963.
- Stoll, R., Gibbs, J. A., Salesky, S. T., Anderson, W., and Calaf, M.: Large-Eddy Simulation of the Atmospheric Boundary Layer, Boundary-Layer Meteorology, 177, 541–581, https://doi.org/10.1007/s10546-020-00556-3, https://doi.org/10.1007/s10546-020-00556-3, 2020.
 - van Heerwaarden, C. C., van Stratum, B. J. H., Heus, T., Gibbs, J. A., Fedorovich, E., and Mellado, J. P.: MicroHH 1.0: A Computational Fluid Dynamics Code for Direct Numerical Simulation and Large-Eddy Simulation of Atmospheric Boundary Layer Flows, Geoscientific Model Development, 10, 3145–3165, https://doi.org/10.5194/gmd-10-3145-2017, https://gmd.copernicus.org/articles/10/3145/2017/gmd-10-3145-2017-discussion.html, 2017.
 - Verstappen, R.: When Does Eddy Viscosity Damp Subfilter Scales Sufficiently?, Journal of Scientific Computing, 49, 94, https://doi.org/10.1007/s10915-011-9504-4, https://doi.org/10.1007/s10915-011-9504-4, 2011.
 - Wang, Y., MacCall, B. T., Hocut, C. M., Zeng, X., and Fernando, H. J. S.: Simulation of Stratified Flows over a Ridge Using a Lattice Boltzmann Model, Environmental Fluid Mechanics, 20, 1333–1355, https://doi.org/10.1007/s10652-018-9599-3, https://doi.org/10.1007/s10652-018-9599-3, 2020.
 - Wu, K. and Porté-Agel, F.: Flow Adjustment Inside and Around Large Finite-Size Wind Farms, Energies, 10, 2164, https://doi.org/10.3390/en10122164, http://www.mdpi.com/1996-1073/10/12/2164, 2017.
- Yang, X., Mehmani, Y., Perkins, W. A., Pasquali, A., Schönherr, M., Kim, K., Perego, M., Parks, M. L., Trask, N., Balhoff, M. T., Richmond, M. C., Geier, M., Krafczyk, M., Luo, L.-S., Tartakovsky, A. M., and Scheibe, T. D.: Intercomparison of 3D Pore-Scale Flow and Solute Transport Simulation Methods, Advances in Water Resources, 95, 176–189, https://doi.org/10.1016/j.advwatres.2015.09.015, https://www.sciencedirect.com/science/article/pii/S0309170815002225, 2016.
 - Yang, X. I. A., Park, G. I., and Moin, P.: Log-Layer Mismatch and Modeling of the Fluctuating Wall Stress in Wall-Modeled Large-Eddy Simulations, Physical Review Fluids, 2, 104 601, https://doi.org/10.1103/PhysRevFluids.2.104601, https://link.aps.org/doi/10.1103/PhysRevFluids.2.104601, 2017.